Journal Pre-proof

Mechanochemical synthesis and characterization of nanocrystalline $Ni_{1-x}Co_xFe_2O_4$ ($0 \leq x \leq 1$) ferrites

Jhon A. Castrillón Arango, Adrián A. Cristóbal, Cinthia P. Ramos, Paula G. Bercoff, Pablo M. Botta

PII: S0925-8388(19)33290-6

DOI: https://doi.org/10.1016/j.jallcom.2019.152044

Reference: JALCOM 152044

To appear in: *Journal of Alloys and Compounds*

Received Date: 24 May 2019

Revised Date: 14 August 2019

Accepted Date: 26 August 2019

Please cite this article as: J.A. Castrillón Arango, Adriá.A. Cristóbal, C.P. Ramos, P.G. Bercoff, P.M. Botta, Mechanochemical synthesis and characterization of nanocrystalline $Ni_{1-x}Co_xFe_2O_4$ ($0 \leq x \leq 1$) ferrites, *Journal of Alloys and Compounds* (2019), doi: https://doi.org/10.1016/j.jallcom.2019.152044.

MECHANOCHEMICAL SYNTHESIS AND CHARACTERIZATION OF NANOCRYSTALLINE $Ni_{1-x}Co_xFe_2O_4$ ($0 \leq x \leq 1$) FERRITES

Jhon A. Castrillón Arango[a], Adrián A. Cristóbal[a], Cinthia P. Ramos[b], Paula G. Bercoff[c], Pablo M. Botta[a]

[a] Instituto de Investigaciones en Ciencia y Tecnología de Materiales (INTEMA), UNMdP-CONICET, J. B. Justo 4302, B7608FDQ Mar del Plata, Argentina.

[b] Instituto de Nanociencia y Nanotecnología (INN), CNEA-CONICET, Buenos Aires, Argentina. Departamento de Física de la Materia Condensada, GIyA-CNEA. Avenida General Paz 1499, (1650) San Martín, Buenos Aires, Argentina.

[c]Facultad de Matemática, Astronomía, Física y Computación (FaMAF), Universidad Nacional de Córdoba, Instituto de Física Enrique Gaviola (IFEG), CONICET, Medina Allende s/n, Ciudad Universitaria, Córdoba, Argentina.

Abstract

Magnetic ferrites $Ni_{1-x}Co_xFe_2O_4$ are synthesized by means of a simple, clean and scalable route consisting of a solid-state reaction induced by high energy ball-milling between metal salts (Lewis'acids) and sodium hydroxide (base). The chemical reaction occurs at room temperature and produces nanocrystalline $Ni_{1-x}Co_xFe_2O_4$ and soluble byproducts, which are efficiently removed by washing. Thermal treatments at several temperatures are performed to favor the crystallization of the desired phase. The evolution of the system with mechanochemical reaction and heating is followed by X-ray diffraction, Raman spectroscopy, thermal analyses and scanning electron microscopy. The magnetic properties of the obtained ferrites are studied by Mössbauer spectroscopy and vibrating sample magnetometry. The adequate combination of mechanochemical and thermal treatments leads to obtain pure materials with excellent magnetic properties, depending on the composition, the particle size, the cation distribution and the canted spin structure at the surface of the nanoparticles.

Keywords: Ferrite; Magnetic Ceramics; Mechanochemistry; Spinels; Nanoparticles

Introduction

The term ferrite is commonly used to describe a family of magnetic oxide compounds containing iron oxide as a main component. In fact, magnetite (Fe_3O_4) is a conspicuous member of this family and was the first known magnetic material [1]. Ferrites can adopt three different crystal lattices: spinel ferrites (cubic), hexaferrites (hexagonal) and garnets (cubic). Each structure gives rise to characteristic magnetic properties, which in turn may change according to the chemical composition and ordering of the ions within the crystal lattice [2]. In particular, spinel ferrites have a general formula AFe_2O_4, where A are divalent ions, such as Fe^{2+}, Cu^{2+}, Zn^{2+}, Mg^{2+}, etc. The crystal structure can be described as a cubic close-packed arrangement of O^{2-} anions, where cations occupy tetrahedral and octahedral sites. In normal spinels, divalent cations occupy one-eighth of the tetrahedral sites and one-half of the octahedral sites are occupied by Fe^{3+} ions. Inverse spinel ferrites are better expressed by writing $Fe^{3+}(AFe^{3+})O_4$, indicating that half of the Fe^{3+} ions occupy tetrahedral sites and the remaining half, together with the A^{2+} ions, occupy the octahedral interstitials. Between these two structural models there exist spinel ferrites with a variable cation distribution, which can be represented by the general formula $(A^{2+}_{(1-\delta)}, Fe^{3+}_{\delta})^{tet}[A^{2+}_{\delta}, Fe^{3+}_{(2-\delta)}]^{oct}O_4$, where δ is the inversion degree of the spinel [3].

In the last decades, ferrite-based materials have drawn interest for a plethora of applications, such as catalysts and gas sensors [4,5], data storage [6,7], microwave devices [8], in biomedical applications (contrast agents in RMN and magnetic-guided devices) [9,10], etc. Besides their well-known magnetic properties, spinel ferrites are also investigated because of their interesting photocatalytic properties [11]. Absorption of visible radiation by ferrite nanoparticles facilitates photocatalytic processes, for example in degradation of water pollutants, being possible to achieve the magnetic separation of these particles after using [12,13].

Amongst all the spinel ferrites, $CoFe_2O_4$ has a partially inverse structure and it is a well-known hard magnetic material, with relatively high values of saturation magnetization and coercivity. $NiFe_2O_4$ is a completely inverse spinel and it behaves as a soft magnetic material (with high saturation magnetization and low coercivity) [14]. These properties make these ferrites very promising candidates for a variety of applications in biomedical, electronic as

well as recording technology [15–17]. Moreover, Ni–Co ferrites are important electronic materials, which are used in electronic devices suited for high-frequency applications in the telecommunication field [18]. These materials are commercially used in high-quality filters, rod antenna radio frequency circuits, transformer cores, read/write heads for high-speed digital tape and operating devices [19, 20].

Because of the extensive applicability of spinel ferrites, various synthesis routes have been developed since their discovery. These include the classical solid-sate reaction, sol–gel [21–23], co-precipitation [24,25], hydrothermal [26], microemulsion [27], plasma or microwave treatment [28,29], host template [30,31] and others. Some of the preparative methods have been focused on the fabrication of nanometric particles, with superparamagnetic behavior.

In the last decades, mechanochemically assisted synthesis has become a reliable tool for preparing a variety of inorganic and organic materials [32,33]. Some advantages of this method are the relative simplicity of the process, the use of common precursors (metal oxides or salts), the absence of organic solvents and the possibility of obtaining metastable phases with different properties to those of the conventionally prepared materials. The use of a mechanochemical procedure to modify the structure and properties of spinel ferrites dates back to the '80s, when Ni and Zn ferrites were investigated [34,35]. Some years later, several articles reporting the synthesis of spinel ferrites appeared, mainly with the aim to study the effect of mechanosynthesis on the magnetic properties and the possibility to obtain nanoparticles of these materials [36-39]. McCormick et al. developed an alternative mechanochemical route to obtain a variety of nanometric single oxides, such as ZnO, Fe_2O_3, Al_2O_3, TiO_2, etc [40-44]. The method is based on an acid-base reaction between metal salts and inorganic bases, to produce nanocrystalline oxides mixed with a water soluble byproduct, which can be easily removed by washing. Although this preparative technique has been extensively used in the synthesis of single oxides, its application to complex oxides is really scarce [45,46]. Some of the authors of the present article have reported two previous studies about multiferroic nanocrystalline orthoferrites, synthesized by McCormick's method, showing the effect of the mechanochemical activation in the cation distribution and its influence on the hyperfine structure and magnetic properties [47,48]. In this work, we apply this synthetic route to spinel ferrites, in order to develop a

facile and clean preparation route for these materials, and to investigate the differences in formation of crystal structures, cationic distribution and magnetic orderings from those conventionally obtained.

Experimental

Starting materials were $FeCl_3.6H_2O$ (commercial reagent, 99%), $Co(Ac)_2.4H_2O$ (commercial reagent, 99.9 %), $Ni(Ac)_2.4H_2O$ (commercial reagent, 99.9 %), and NaOH (commercial reagent, 99 %) . The reactants were mixed according to the stoichiometry of reaction (1), with x = 0.0, 0.3, 0.5, 0.7 and 1.0. These mixtures were milled under air atmosphere during 2 h in a planetary ball-mill Fritsch Pulverisette 7, using vials (45 cm^3) and balls (15 mm in diameter) made of silicon nitride. A ball-to-powder mass ratio of 4 and a rotation speed of 700 rpm were used.

$$(1\text{-}x)Ni(Ac)_2.4H_2O + xCo(Ac)_2.4H_2O + 2FeCl_3.6H_2O + 6NaOH + 4O_2 \rightarrow Ni_{1-x}Co_xFe_2O_4 + 6\,NaCl + 4CO_2 + 22H_2O \quad (1)$$

After milling, the samples were washed by stirring with distilled water to remove the soluble by-products. The obtained powders were filtered and dried at 60ºC and then calcined for 1 h at temperatures between 600 and 900ºC. The resulting samples were labeled as NCF-x-y, being x the Co content and y the calcination temperature.

X-ray diffraction (XRD) was used to follow the phase evolution during mechanochemical and thermal treatments with an X'Pert PRO PANalytical diffractometer, equipped with a graphite monochromator, using CuKα radiation (λ= 1.5406 Å) at 40 kV and 40 mA. A scan range of 10-80° 2θ and a step size of 0.02° were used. Lattice parameters (*a*) were calculated according to equation (2) for cubic systems, using interplanar distances (*d*) corresponding to plane (3 1 1), while Scherrer's equation was used in order to estimate crystallite sizes [49].

$$\frac{1}{d^2} = \frac{h^2+k^2+l^2}{a^2} \quad (2)$$

The microstructure and elemental composition of the samples was examined in a scanning electron microscope (SEM) Sigma Zeiss with field emission gun and an Oxford detector for X-ray emission spectroscopy (LAMARX facilities). TEM analyses were performed using a JEOL (JEM-2100) microscope with a voltage of 120 kV. Previously to the observation, the samples were suspended in Cu grids.

Thermogravimetric analyses (TGA) were performed in a Shimadzu TGA-50H instrument under flowing air, using a heating rate of 10ºC/min and approximately 20 mg of sample mass.

Raman spectroscopy was performed at room temperature using an Invia Reflex confocal Raman microprobe with Ar^+ laser of 514 nm in backscattering mode, with a laser spot of 10 μm. An exposure time of 20 s and 3 accumulations were used, with a 50X objective. The laser power was reduced to 10% to prevent damage by heating (0.2 mW).

Mössbauer spectra were taken at room temperature (RT) with a conventional constant acceleration spectrometer in transmission geometry with a ^{57}Co/Rh source. The absorber thickness was chosen to be the optimum according to the Long et al. criterion [50]. Least-squares fitting of the spectra were performed by using the Normos program [51]. Isomer shift (IS) values are given relative to that of α-Fe at RT.

Magnetization (M) as a function of magnetic field (H) was measured in a vibrating sample magnetometer Lakeshore 7300. Hysteresis loops were registered at RT for all the heated samples.

Results and discussion

Figure 1 shows XRD diagrams of the as-milled samples for compositions x = 0 and x = 1, NCF-0.0 and NCF-1.0 respectively. High intensity peaks belonging to NaCl and NaAc are observed, indicating the occurrence of a chemical reaction during the mechanical treatment. There is no evidence of remaining reactants or formation of the ferrite phase. The mechanochemical treatment produced an acid-base reaction with the formation of sodium salts, although the oxidation of acetate groups to CO_2 is not confirmed. TGA curves for samples with x = 0 and x = 1 (inset of Figure 1) show two thermal events at 100 and 300-360ºC, corresponding to loss of water and CO_2 in $Ni(Ac)_2.4H_2O$ and $Co(Ac)_2.4H_2O$. A total

mass loss of 35-36 % agrees with the loss undergone by metallic acetates when produced by oxidation of CO_2 and water. The combination of XRD and TGA results suggests that during the ball-milling an acid-base reaction takes place with formation of NaCl and NaAc. The oxidation of acetate groups to CO_2 requires a thermal treatment of the solid mixtures at least at 400ºC. The absence of diffraction peaks from the spinel $Ni_{1-x}Co_xFe_2O_4$ evidences the very low crystallinity of the formed product, as a consequence of the synthesis conditions (high-energy ball milling and room temperature) which difficult the crystallization of ferrite phases. Taking into account these observations, calcination temperatures were selected from 600 to 800ºC.

Figure 2 displays the diffractograms for sample NCF-0.5, calcined at 600, 700 and 800ºC. The complete formation of $Ni_{0.5}Co_{0.5}Fe_2O_4$ is observed already at 600ºC. For higher temperatures, an improved crystallinity can be noticed, shown by the increase of intensity and sharpening of the peaks. There is no evidence of impurities or secondary phases in any of the samples. Lattice parameters and crystallite sizes are listed in Table 1. As expected, an increase in crystallite size with heating temperature is observed.

Magnetic hysteresis loops for sample NCF-0.5 heated at 600, 700 and 800ºC are shown in Figure 3. The typical magnetic behavior for soft magnetic materials can be observed, achieving magnetic saturation at very low applied fields, relatively high saturation magnetization (Ms) values and very low coercivities (Hc). It is a well-known fact that for spinel ferrites the main contribution to magnetism is the spin magnetic moment of transition metal cations Fe^{3+}, Co^{2+} and Ni^{2+}. The observed net magnetization is the result of the magnetic moment of each cation and its distribution among the different sites into the spinel structure. Thermal treatments at higher temperatures increase magnetization values, changing from 46.5 emu/g (600ºC) to 62.3 emu/g (800ºC). Temperature induces the formation of larger and more crystalline grains, enhancing the magnetization. The inset shows the almost linear variation of saturation magnetization with heating temperature. Coercivity also shows a similar tendency with T, increasing about 50% between 600 and 800ºC. As shown in Table 2, the obtained values of Ms and Hc for sample NCF-0.5-800 agree with those previously reported for $Ni_{0.5}Co_{0.5}Fe_2O_4$ synthesized by other methods [28, 52-57]. It is important to remark that from the vast existing literature on this mixed ferrite, only reports dealing with materials with similar particle size and heating temperatures were

selected for the comparison. The effect of composition on magnetism is further investigated by Raman spectroscopy and VSM (see Figs. 8 and 9)

Considering the previous results, a calcination temperature of 800^{o}C was selected for all the compositions of the mechanosynthesized Ni-Co ferrites. Figure 4 shows XRD patterns for the series of samples NCF-x-800. All the diffractograms reveal the formation of the crystalline ferrite phase and the absence of impurities, since all the observed peaks correspond to the cubic spinel structure, matching the JCPDS-PDF 22-1086 and 10-0325 standards (parent compounds). As Co content (x) increases, a shift of peak positions to lower angles can be observed (the inset clearly displays this effect for reflection (3 1 1), corresponding to the most intense peak). This observation indicates an expansion of the unit cell as x increases, due to the larger ionic radium of Co^{2+} [58] compared to that of Ni^{2+}. Table 3 shows the increase of lattice parameter and cell volume with cobalt content. Moreover, an increasing trend of crystallite size with x can be noticed, which may be related to the fact that Co^{2+} could accelerate the relative nucleation rate and crystal growth [56-59].

The nominal composition of the samples calcined at 800ºC was corroborated with X-ray emission spectroscopy. An excellent agreement with the real composition was found, as shown in Table 3.

The samples' microstructures are shown in Figure 5 (SEM) and 6 (TEM). SEM images show agglomerated nanoparticles with an irregular surface morphology. The effect of temperature is evidenced in the images of samples NCF-0.5-600 (Fig.5a) and NCF-0.5-800 (Fig. 5b). An increase of the average particle size from 30 nm to 50 nm is observed in the analyzed temperature range. Figures 5b, 5c and 5d reveal the influence of composition on the particle size (at the same calcination temperature, 800ºC). As the Co content grows, a size increment can be observed, in agreement with the variation observed for the crystallite size (Table 3). TEM images of these samples (Figure 6) allow determining a more prismatic morphology of the nanoparticles, confirming the particle size observed by SEM and its increasing trend with Co content (x). Indeed, the values of crystallite size estimated with Scherrer's equation are very close to the particle sizes observed by electron

microscopy. This suggests that the nanoparticles are mostly formed by single crystalline domains, as Figure 6 reveals.

Raman spectra for some of the obtained ferrites are displayed in Figure 7 (a) to (d), with the corresponding deconvolutions, performed with the software Origin 8.1.

The five first-order Raman active modes predicted by Group theory for perfectly inverse spinel ferrites are noticeable in all the curves, in the 100-800 cm^{-1} range [60]. The modes below 600 cm^{-1} ($T_{2g}(3)$ at ~ 190 cm^{-1}; E_g at ~ 320 cm^{-1}; $T_{2g}(2)$ at ~ 475 cm^{-1} and $T_{2g}(1)$ at ~ 565 cm^{-1}) are related to the vibrations in octahedral sites (O-modes), while the modes above this frequency ($A_g(1)$ at ~ 695 cm^{-1}) are ascribed to phonons in the tetrahedral sublattice (T-modes) [61, 62]. After deconvoluting the spectra with Lorentzians for every peak, a close inspection leads to the realization that some extra modes appear, mainly around the $A_g(1)$ band. This feature has already been observed in Co ferrite prepared by the sol-gel combustion method [63] and it was explained considering that the spinel is not perfectly inverse due to an inhomogeneous cation distribution, thus giving rise to extra phonon vibrations in the tetrahedral sites and a very small O-mode that arises around 360 cm^{-1}.

It is evident from comparing Figure 7 (a) and Figure 7 (c) that increasing the calcining temperature of sample NCF-0.5 from 600^{o}C to 800^{o}C produces a systematic blue-shift in all the peaks, to the positions expected for more ordered spinels. This is probably because a more energetic thermal treatment promotes more crystalline structure, in agreement with XRD and magnetization results.

Substituting Co for Ni in the formulation $Ni_{1-x}Co_xFe_2O_4$ does not alter significantly the position of the main five peaks, but it modifies the corresponding to the new bands around the $A_g(1)$ band (displayed with solid (orange) lines in the spectra of Figure 7). This is in agreement with the assignment of these peaks to the particular cation distribution in the spinel, which is not perfectly inverse [63]. The Raman spectrum of NCF-0.0-800 (nickel ferrite) shown in Figure 7 (d) displays a blue-shift in all its peaks with respect to the spectrum of cobalt ferrite (NCF-1.0-800, shown in Figure 7 (b)). As explained by Kumar et al. [64] this shift is because the atomic mass of Ni ion (58.693 g) is lower than that of Co ion (58.933 g).

Mössbauer analysis was performed in order to investigate the effect of Ni and Co ions on the hyperfine properties of the ferrite nanoparticles. Figure 8 displays the Mössbauer spectra measured at RT for samples NCF-x-800; the corresponding hyperfine parameters are shown in Table 4.

The spectra were fitted to three sextets, one of them characteristic of Fe ions in high spin trivalent state -Fe^{3+}- at tetrahedral position (A-site) and the other two denoting Fe^{3+} at octahedral positions (B and B1-sites). There is no evidence for the presence of Fe^{2+}, which confirms the stoichiometry of the samples. These features can be deduced from the isomer shift (IS) values.

In a Mössbauer study of nanosized Co-Ni ferrites synthesized by the PVA sol-gel method [65], the authors fit the spectra with only two subspectra, one for tetrahedral and one for octahedral sites; but in our case a more accurate fit was done with one subspectra for tetrahedral and two for octahedral sites, in accordance to other authors who found more than one octahedral site for different cation substituted ferrites [66,67]. The use of an external magnetic field and low temperature spectra are sometimes necessary to perform a proper distinction between the contributions from tetrahedral and octahedral sites, due to a strong overlapping of lines in both cases. However, our spectra at RT allowed distinguishing the contribution of each lattice sites in order to roughly analyze the magnetic behavior.

The Fe^{3+} ions are distributed over A, B and B1 sites, showing a slight preference towards tetrahedral (A) sites in most of the samples (see Table 4). This is in agreement with the analysis derived from Raman results. It is known that Ni^{2+} ions have a preference for octahedral sites, while Co^{2+} and Fe^{3+} ions can occupy both octahedral and tetrahedral sites [54]. Fe^{3+} ions tend to occupy tetrahedral sites when the Co^{2+} concentration increases, as deduced from the comparison of the fraction of Fe^{3+} in tetrahedral sites relative to those in octahedral sites ($f_A/(f_B + f_{B1})$ in Table 4) for the mixed substituted samples. For the parent compounds (NCF-0.0-800 and NCF-1.0-800), the fraction of iron cations on A sites equates. The hyperfine parameters are also very similar for those samples, probably due to the influence of other factors such as particle size and surface effects.

The two local magnetic fields for the Fe^{3+} octahedral sites (B and B1), with different $2\varepsilon_Q$ values, are assigned to different distortions of the octahedral environment. The zero value for $2\varepsilon_Q$ in B sites suggests a symmetrical octahedral site meanwhile that in B1 points out to a lower symmetry site. This change is due to the variation in the angles between the principal axis of the electric field gradient and the spin direction. This fact let us infer that spin canting exists at B1 sites-associated with Fe^{3+} ions at octahedral sites (probably in the surface of the nanoparticles) [67]. With Co addition, there is an increment of the B1 area fraction of the mixed substituted samples, denoting a higher fraction of canted spins (Table 3). Even if spin canting tends to lower the magnetic moment, the net magnetization increases as can be seen further below in the magnetization measurement analysis (Fig. 9). This effect is likely related to the cationic distribution in the surface of the nanoparticles. When Co concentration is 0.0 (NCF-0.0-800), the fraction of A, B and B1 sites equals that of NCF-1.0-800; however Ms is higher for NCF-1.0-800 due to the magnetic moment of Co^{2+} (3 μ_B) compared to that of Ni^{2+}(2 μ_B) and to the nanoparticle sizes (there is a visible increment of nanoparticle size in NCF-1.0-800 compared to that of NCF-0.0-800, see SEM and TEM results).

The hyperfine magnetic field values (B_{hf}) at A sites seem to remain rather constant, meanwhile B_{hf} values at B sites slightly increase when Ni^{2+} ions are substituted by Co^{2+} ions. This can be explained by the weakening of the superexchange interactions due to the above described cation distribution and to the spin canting in the surface of the nanoparticles. As a consequence, there is an increase in coercivity and magnetization (see discussion below) and therefore in anisotropy, when Co content increases. These results show that aside from interactions, surface and size effects, the occupancy of octahedral B and B1 sites is crucial to define the magnetic properties of the studied ferrite nanoparticles being also closely related to the spin structure.

The magnetic behavior at RT of the series of samples NCF-x-800 is shown in Figure 9. As Co content grows, a significant increase of Ms and Hc can be observed. In general, the registered values are in good agreement with those reported previously (see Table 1). From a fundamental point of view, Co^{2+} ions have a higher magnetic moment than Ni^{2+} ions (3 μ_B and 2 μ_B, respectively). Assuming that Co^{2+} ions occupy the same sites of Ni^{2+} ions, a

linear increase of magnetization with x is expected, as can be observed up to x = 0.5. For Co^{2+} contents higher than 0.5, a faster increase of Ms is evidenced. This could be related with the occupation of tetrahedral sites by Co^{2+} ions, taking into account the partially inverse spinel-structure predicted for $CoFe_2O_4$. Coercivity values also increase with Co content, steeply up to x = 0.5 and mildly from x = 0.5 to x = 1. It is well-known that the magnetocrystalline anisotropy of $CoFe_2O_4$ is higher than that of other spinel ferrites, such as $NiFe_2O_4$. This explains the higher Hc values measured for the compositions richer in Co.

For NCF-1.0-800 nanoparticles, the saturation magnetization (Ms) is 87.7 emu/g and for NCF-0.0-800 it is 46.1 emu/g. These values are slightly lower than the bulk values measured at room temperature reported in literature (93.9 emu/g and 50.0 emu/g, respectively). The decrease may be attributed to the canted spin structure and spin non-collinearity at the surface of the nanoparticles.

Conclusions

The mechanochemical treatment of acid salts and sodium hydroxide produced the formation of poorly crystalline $Ni_{1-x}Co_xFe_2O_4$ together with soluble byproducts. Pure and nanocrystalline ferrites with average particle and crystallite sizes between 30 and 50 nm were obtained by successively heating and washing of the milled powders.

The analysis of the Mössbauer spectra revealed the existence of two local magnetic fields for the Fe^{3+} octahedral sites, which were assigned to different distortions of the octahedral environment (symmetrical and non-symmetrical sites).

The magnetic properties are found to vary with the particle size, the magnetic interactions but mainly with the cation distribution, which in turn is associated to the canted spin structure at the surface of the nanoparticles.

The proposed mechanosynthesis method proved to be an efficient, clean, scalable and low-cost route to obtain magnetic nanocrystalline materials with singular structural features. An adequate control of the synthesis variables (milling conditions and heating temperature) should allow tuning the magnetic properties, according to a selected specific application.

Acknowledgements

The authors wish to thank CONICET, UNMdP, ANPCyT for the financial support given to this work. J. A. Castrillón Arango specially acknowledges ANPCyT for the conceded fellowship.

References

1. U. Enz, Magnetism and Magnetic Materials: Historical Developments andPresent Role in Industry and Technology.Handbook of Magnetic Materials, Vol. 3. North-Holland, 1982.

2. U.S.R.M Cornell,The Iron Oxides: Structure, Properties, Occurrences and Uses, Weinheim: Wiley-VCH, 2003.

3. M. Sugimoto, The Past, Present, and Future of Ferrites. J. Am. Ceram. Soc., 82 (1999) 269–80.

4. K.V.S. Ranganath, M.Shaikh, A.Sahu, G.Sarvani, Catalytic Activity of Functionalized Spinels. Curr. Org. Chem. 21 (2017) 2573–2584.

5. A. Sutka, K.A. Gross, Spinel ferrite oxide semiconductor gas sensors. Sens.Actuators B 222 (2016) 95–105.

6. M. Ismail, A. Hao, W. Huang, J. Lee, S. Kim, D.Bao, Coexistence of unipolar and bipolar switching in nanocrystalline spinel ferrite $ZnFe_2O_4$ thin films synthesized by sol-gel method. Appl. Phys. Lett. 113 (2018) 152103.

7. S.F. Mansour, M.A. Abdo, S.M. Alwan, The role of Cr^{3+} ions substitution on structural, magnetic and dielectric modulus of manganese zinc nanoferrites. Ceramics International 44 (2018) 8035–8042.

8. R. Ahmad, I.H. Gul, M. Zarra, H. Anwar, M. B. Niazi, A. Khan, Improved electrical properties of cadmium substituted cobalt ferrites nano-particles for microwave application. J. Magn. Magn. Mater. 405 (2016) 28–35.

9. A.K. Gupta, M. Gupta .Synthesis and surface engineering of iron oxide nanoparticles for biomedical applications. Biomaterials 26 (2005) 3995–4021.

10. L. Mohammed, H.G. Goma, D. Ragab, J. Zhu. Magnetic nanoparticles for environmental and biomedical applications: A review. Particuology 30 (2017) 1–14.

11.E. Casbeer, V.K. Sharma, X-. Li, Synthesis and photocatalytic activity of ferrites under visible light: A review. Sep. Pur. Technol. 87 (2012) 1–14.

12. K.K. Kefeni, B.B. Mamba, T.A.M. Msagati, Application of spinel ferrite nanoparticles in water and wastewater treatment: A review. Sep. Pur, Technol. 188 (2017) 399-422

13. G. Mamba, A. Mishra. Advances in Magnetically Separable Photocatalysts: Smart, Recyclable Materials for Water Pollution Mitigation. Catalysts 6 (2016) 79.

14. J. Smit, H. P. J. Wijn, Ferrites, Philips Technical Library, Eindhoven, The Netherlands, 1959.

15. S.Y.Srinivasan, K. M.Paknikar, D.Bodas, V. Gajbhiye, Applications of cobalt ferrite nanoparticles in biomedical nanotechnology. Nanomedicine 13 (2018) 1221–38.

16. T. Zhou, T. Zhang, Y. Zeng, R. Zhang, Z. Lou, J. Deng, L. Wang, Structure-driven efficient $NiFe_2O_4$ materials for ultra-fast response electronic sensing platform, Sens. Actuators B 255 (2018) 1436–1444.

17. Q. Dai, D. Berman, K. Virwani, J.Frommer, P.-O.Jubert, M. Lam, T. Topuria, W. Imaino, A. Nelson, Self-Assembled Ferrimagnet−Polymer Composites for Magnetic Recording Media, Nano Lett. 10 (2010) 3216–3221.

18. A. Goldman, Modern Ferrite Technology, Van Nostrand Reinhold, NY, 1990.

19. V.L. Mathe, R.B. Kamble, Electrical and dielectric properties of nano crystalline Ni–Co spinel ferrites, Mater. Res. Bull. 48 (2013) 1415–1419.

20. C. Stergiou, Magnetic, dielectric and microwave absorption properties of rare earth doped Ni–Co and Ni–Co–Zn spinel ferrites, J. Magn. Magn. Mater. 426 (2017) 629–635.

21. A. Kumar, P. Sharma, D. Varshney, Structural, vibrational and dielectric study of Ni doped spinel Co ferrites: $Co_{1-x}Ni_xFe_2O_4$ (x=0.0, 0.5,1.0), Ceram. Int. 40 (2014) 12855–12860.

22. S.B. Waje, M. Hashim, W. D. Wan Yusoff, Z. Abbas, X-ray diffraction studies on crystallite size evolution of $CoFe_2O_4$ nanoparticles prepared using mechanical alloying and sintering, Appl. Surf. Sci. 256 (2010) 3122–3127.

23. A. Sutka, G. Mezinskis, Sol–gel auto-combustion synthesis of spinel-type ferrite nanomaterials, Front. Mater. Sci. 6 (2012) 128–141.

24. X. Huang, J. Zhang, W. Wang, T. Sang, B. Song, H. Zhu, W. Rao, C. Wong, Effect of pH value on electromagnetic loss properties of Co–Zn ferrite prepared via coprecipitation method, J. Magn. Magn.Mater. 405 (2016) 36–41.

25. K. Maaz, W. Khalid, A. Mumtaz, S.K. Hasanain, J. Liu, J.L. Duan, Magnetic characterization of $Co_{1-x}Ni_xFe_2O_4$ ($0<x<1$) nanoparticles prepared by co-precipitation route, PhysicaE41 (2009) 593–599.

26. R.S. Melo, P. Banerjee, A. Franco, Hydrothermal synthesis of nickel doped cobalt ferrite nanoparticles: optical and magnetic properties, J. Mater. Sci: Mater Electron 29 (2018) 14657–67.

27. M. Hashim, S.E. Shirsath, S.S. Meena, M.L. Mane, S. Kumar, P. Bhatt, R. Kumar, N.K. Prasad, S.K. Alla, J. Shah, R.K. Kotnala, K.A. Mohammed, E. Şentürk, Alimuddin, Manganese ferrite prepared using reverse micelle process: Structural and magnetic properties characterization, J. Alloys Compd. 642 (2015) 70–77.

28. A.B. Nawale, N.S. Kanhe, S.A. Raut, S.V. Bhoraskar, A.K. Das, V.L. Mathe, Investigation of structural, optical and magnetic properties of thermal plasma synthesized Ni-Co spinel ferrite nanoparticles, Ceram. Int. 43 (2017) 6637–6647.

29. Z. Ai, K. Deng, Q. Wan, L. Zhang, S. Lee, Facile Microwave-Assisted Synthesis and Magnetic and Gas Sensing Properties of Fe_3O_4 Nanoroses, J. Phys. Chem. C 114 (2010) 6237–6242.

30. M.S. El-Sheikh, F.A. Harraz, M.M. Hessien, Magnetic behavior of cobalt ferrite nanowires prepared by template-assisted technique, Mater. Chem. Phys. 123 (2010) 254–259.

31. K. Niu, L. Liang, F. Peng, F. Zhang, Y. Gu, H. Tian, Chelating-Template-Assisted in Situ Encapsulation of Zinc Ferrite Inside Silica Mesopores for Enhanced Gas-Sensing Characteristics, Appl. Mater. Interfaces 8 (2016) 24682-24691.

32. S.L. James,C.J. Adams, C. Bolm, D. Braga, P. Collier et al., Mechanochemistry: opportunities for new and cleaner synthesis, Chem. Soc. Rev., 41 8 (2012) 413–447.

33. M. Klimakow, P. Klobes, A. F. Thüunemann, K. Rademann, F. Emmerling, Mechanochemical Synthesis of Metal-Organic Frameworks: A Fast and Facile Approach toward Quantitative Yields and High Specific Surface Areas, Chem. Mater. 22 (2010) 5216–5221.

34. Yu.T. Pavljukhin, Ya.Ya. Medikov, V.V. Boldyrev, Magnetic and chemical properties of mechanically activated zinc and nickel ferrites, Mat. Res. Bull. 18 (1983) 1317-1327.

35. Yu.T.Pavljukhin, Ya.Ya.Medikov, V.V.Boldyrev, On the consequences of mechanical activation of zinc and nick el ferrites, J. Solid State Chem. 53 (1984) 155-160.

36. C. Jovalekic, M. Zdujic, A. Radakovic, M. Mitric, Mechanochemical synthesis of $NiFe_2O_4$ ferrite, Mater.Lett. 24 (1995) 365–368.

37. W. Kim, F. Saito, Mechanochemical synthesis of zinc ferrite from zinc oxide and α-Fe_2O_3, Powder Technol. 114 (2001) 12–16.

38. V. Sepelák, D. Baabe, D. Mienert, F.J. Litterst, K.D. Becker, Structural Disorder in the High-Energy Milled Magnesium Ferrite, J. Appl. Phys. 88 (2000) 5884–5893.

39.V. Sepelák, A. Düvel, M. Wilkening, K.D. Becker, P. Heitjans, Mechanochemical reactions and syntheses of oxides, Chem. Soc. Rev. 42 (2013) 7507–7520.

40. A.C. Dodd, Nanocrystalline zirconia powders synthesised by mechanochemical processing, Mater. Sci. Eng. A301 (2001) 54–58.

41. T. Tsuzuki, P.G. McCormick, Synthesis of Ultrafine Ceria Powders by Mechanochemical Processing, J. Am. Ceram. Soc., 84 (2001)1453–58.

42. P.G. McCormick, T. Tsuzuki, J.S. Robinson, J. Ding, Nanopowders Synthesized by Mechanochemical Processing, Adv. Mater. 13 (2001) 1008–1010.

43. T. Tsuzuki, P.G. McCormick, Mechanochemical synthesis of nanoparticles, J. Mater. Sci. 39 (2004) 5143 – 5146.

44. T. Tsuzuki, F. Schäffel, M. Muroi, P.G. McCormick, Magnetic properties of mechanochemically synthesized γ-Fe_2O_3 nanoparticles, J. Alloys Compd. 509 (2011) 5420–5425.

45. M. Muroi, P.G. McCormick, R. Street, Surface spin disorder and exchange bias in $La_{0.7}Ca_{0.3}MnO_3$ nanoparticles synthesized by mechanochemical processing, Rev. Adv. Mater. Sci. 5 (2003) 76–81.

46. Y. Todaka, M. Nakamura, S. Hattori, K. Tsuchiya, M. Umemoto, Synthesis of Ferrite Nanoparticles by Mechanochemical Processing Using a Ball Mill, Mater. Trans. 44 (2003) 277–284.

47. A.A. Cristóbal, P.M. Botta, Mechanochemically assisted synthesis of nanocrystalline $BiFeO_3$, Mater. Chem. Phys. 139 (2013) 931–935.

48. A.A. Cristóbal, C.P. Ramos, M.S. Conconi, P.G. Bercoff, P.M. Botta, Structural and magnetic properties of nanocrystalline $Bi_{1-x}La_xFeO_3$ ($0.0 < x < 0.4$) synthesized by a mechanochemical route, Mater. Res. Bull.95 (2017) 292–299.

49. B.D. Cullity, S.R. Stock, Elements of X-ray Diffraction, third ed., Prentice-Hall Inc., New Jersey, 2001.

50. G.J. Long, T.E. Cranshaw, G. Longworth, The ideal Mössbauer effect absorber thickness, Mössbauer Effect Ref. Data J. 6 (1983) 42–49.

51. R.A. Brand, Normos Program, Internat. Rep, AngewandtePhysik, Univ. Duisburg, 1987.

52. M. Mozaffari, J. Amighian, E. Darsheshdar, Magnetic and structural studies of nickel-substituted cobalt ferrite nanoparticles, synthesized by the sol–gel method, J. Magn. Magn.Mater. 350 (2014) 19–22.

53. B. Nandan, M.C.B. Subhash, Static magnetic properties and cation distribution in partially inverse polycrystalline Ni–Co ferrites, Appl. Phys. A. 124 (2018) 756.

54. M.R. de Freitas, G. Lisboa de Gouveia, L.J. Dalla Costa, A.J. A. de Oliveira, R.H.G. A. Kiminami, Microwave Assisted Combustion Synthesis and Characterization of NanocrystallineNickel-doped Cobalt Ferrites, Mater.Res. 19 (2016) 27–32.

55. P.M.A. Caetano, A.S. Albuquerque, L.E. Fernandez-outon, W.A.A. Macedo, Structure , magnetism and magnetic induction heating of $Ni_xCo_{(1-x)}Fe_2O_4$ nanoparticles, J. Alloys Compd. 758 (2018) 247–255.

56. J. Utomo, A. K. Agustina, E. Suharyadi, T. Kato, S. Iwata Effect of Co concentration on crystal structures and magnetic properties of $Ni_{1-x}Co_xFe_2O_4$ nanoparticles synthesized by co-precipitation method, Integrated Ferroelectrics 187 (2018) 194–202.

57. Y. Gao, Y. Zhao, Q. Jiao, H. Li, Microemulsion-based synthesis of porous Co–Ni ferrite nanorods and their magnetic properties, J. Alloys Compd. 555 (2013) 95–100.

58. R.D. Shannon, C.T. Prewitt, Effective ionic radii in oxides and fluorides, Acta Crystallogr. B 25 (1969) 925–946.

59. K. Maaz, A. Mumtaz, S. K. Hasanain, and A. Ceylan, Synthesis and magnetic properties of cobalt ferrite ($CoFe_2O_4$) nanoparticles prepared by wet chemical route, J. Magn. Magn. Mater. 308 (2007) 289–295.

60. P. Graves, C. Johnston, J. Campaniello, Raman scattering in spinel structure ferrites, Mater. Res. Bull. 23 (1988) 1651-1660.

61. Z. Wang, D. Schiferl, Y. Zhao, H.St. C. O'Neill, High pressure Raman spectroscopy of spinel-type ferrite $ZnFe_2O_4$, J. Phys. Chem. Solids 64 (2003) 2517-2523.

62. Y. Qu, H. Yang, N. Yang, Y. Fan, H. Zhu, G. Zou, The effect of reaction temperature on the particle size, structure and magnetic properties of coprecipitated $CoFe_2O_4$ nanoparticles, Mater. Lett. 60 (2006) 3548-3552.

63. I. Haïk Dunn, S. E. Jacobo, P. G. Bercoff, Structural and magnetic influence of yttrium-for-iron substitution in cobalt ferrite, J. Alloys Compd. 691 (2017) 130-137

64. A. Kumar, M. Dar, P. Sharma, D. Varshney, Structural and Raman scattering study of Ni-doped $CoFe_2O_4$, Solid State Phys. (2014) 1148-1150.

65. Z. P. Niu, Y. Wang, and F. S. Li,Mössbauer study of nanosized Co–Ni ferrite $Co_xNi_{1-x}Fe_2O_4$ ($0 < x < 1$) particles, Phys. Status Solidi B 247 (2010)198–201.

66. A. Baykala, Ş. Eryiğit ,Md Amir, H. Güngüneş, H. Sözeri, S.E. Shirsath, M. Sertkol, S.M. Asiri, Magnetic Properties and Cation Distribution of Bimetallic (Mn–Co) Doped $NiFe_2O_4$ Nanoparticles, J. Inorg. Organomet. Polym. 27 (2017) 1893–1900.

67. V. Sepelák, A. Feldhoff, P. Heitjans, F. Krumeich, D. Menzel, F.J. Litterst, I. Bergmann K.D. Becker, Non-equilibrium Cation Distribution, Canted Spin Arrangement, and Enhanced Magnetization in Nanosized $MgFe_2O_4$ Prepared by a One-Step Mechanochemical Route, Chem. Mater. 18 (2006) 3057-3067.

Figure captions

Figure 1. XRD diagrams of as-milled samples NCF-0.0 and NCF-0.1. The inset shows TGA curves for these samples.

Figure 2. XRD diagrams of sample NCF-0.5 heated at 600, 700 and 800ºC.

Figure 3. Magnetization (M) as a function of magnetic field (H) for sample NCF-0.5 calcined at different temperatures. The inset shows saturation magnetization (Ms, open squares, left axis) and coercivity (Hc, solid circles, right axis) as a function of heating temperature.

Figure 4. XRD diagrams of the series of samples NCF-x-800 ($Ni_{1-x}Co_xFe_2O_4$). All the observed peaks correspond to spinel reflections.

Figure 5. SEM images for samples NCF-0.5-600 (a), NCF-0.5-800 (b), NCF-1.0-800 (c) and NCF-0.0-800 (d). Bar: 200 nm.

Figure 6. TEM images for samples NCF-0.0-800 (a), NCF-0.5-800 (b) and NCF-0.1-800 (c)

Figure 7. Raman spectra of selected samples. (a) NCF-0.5-600; (b) NCF-1.0-800; (c) NCF-0.5-800; (d) NCF-0.0-800. All the spectra were fitted with Lorentzians and a linear background, with a regression coefficient R^2=0.996 or better. The five theory-predicted modes are shown with dashed (blue) lines, and the peaks arising from the inhomogeneous cation distribution are displayed with solid (orange) lines.

Figure 8. Mössbauer spectra of the series of samples NCF-x-800.

Figure 9. Magnetization (M) as a function of magnetic field (H) for samples with different Co content (x) calcined at 800 ºC. The inset shows saturation magnetization (Ms) and coercivity (Hc) as a function of x.

Table1. Values of interplanar spacing (d), lattice parameter (a), unit cell volume (V) and crystallite size (t) for sample NCF-0.5 calcined at several temperatures

Sample	d(Å)	a (Å)	V ($Å^3$)	t (nm)
NCF-0.5-600	2.520	8.351	584.1	16
NCF-0.5-700	2.519	8.357	583.6	23
NCF-0.5-800	2.521	8.361	584.6	32

Table 2. Magnetic properties reported for $Ni_{0.5}Co_{0.5}Fe_2O_4$ synthesized by different methods.

Synthesis route	**Temperature (ºC)**	**Particle size (nm)**	**Ms (emu/g)**	**Hc (Oe)**	**Reference**
Sol-gel	500	150	65	760	[46]
Sol-gel	1100	sintered	65	355	[47]
Combustion	Not measured	61	33	941	[48]
Co-precipitation	700	20 *	49	920	[49]
Co-precipitation	90	15 *	12	214	[50]
Thermal plasma	Not measured	30	47	521	[22]
Microemulsion	500	70-80	15	625	[51]
Microemulsion	800	150	45	973	[51]
Mechanochemical	800	32	56	920	Present

* crystallite size

Table 3. Nominal and real Ni:Fe and Co:Fe atomic compositions determined from X-ray spectroscopy results, values of interplanar spacing (d), lattice parameter (a), unit cell volume (V) and crystallite size (t) for the series of samples NCF-x-800.

Sample	Formulation	Nominal Ni:Fe	Real Ni:Fe	Nominal Co:Fe	Real Co:Fe	d(Å)	a (Å)	V (Å^3)	t (nm)
NCF-0.0-800	$NiFe_2O_4$	0.5	0.5	0	0	2.514	8.337	579.5	30
NCF-0.3-800	$Ni_{0.7}Co_{0.3}Fe_2O_4$	0.35	0.37	0.15	0.16	2.518	8.352	582.6	32
NCF-0.5-800	$Ni_{0.5}Co_{0.5}Fe_2O_4$	0.25	0.24	0.25	0.26	2.521	8.361	584.6	32
NCF-0.7-800	$Ni_{0.3}Co_{0.7}Fe_2O_4$	0.15	0.14	0.35	0.35	2.525	8.375	587.4	44
NCF-1.0-800	$CoFe_2O_4$	0	0	0.5	0.49	2.530	8.389	590.4	52

Table 4. Hyperfine parameters.A: tetrahedral sites, B and B1: octahedral sites, IS: isomer shift, $2\varepsilon_Q$: quadrupole shift, B_{hf}: hyperfine magnetic field, f: relative fraction.

Sample	Sites	IS [mm/s]	$2\varepsilon_Q$ [mm/s]	B_{hf} [mm/s]	f (%)	$f_A/(f_B+f_{B1})$
NCF-1.0-800	B	0.36	0.00	52.6	30	1.22
	B1	0.45	0.24	49.7	15	
	A	0.22	-0.03	48.9	55	
NCF-0.7-800	B	0.36	-0.03	52.3	12	1.38
	B1	0.48	0.18	49.2	30	
	A	0.24	-0.05	49.0	58	
NCF-0.5-800	B	0.37	0.00	52.2	22	1.27
	B1	0.42	0.19	49.2	22	
	A	0.24	-0.04	48.9	56	
NCF-0.3-800	B	0.36	0.00	52.3	30	0.96
	B1	0.44	0.17	49.0	21	
	A	0.23	-0.03	48.8	49	
NCF-0.0-800	B	0.36	-0.01	52.4	29	1.22
	B1	0.48	0.21	49.5	16	
	A	0.21	-0.03	48.9	55	

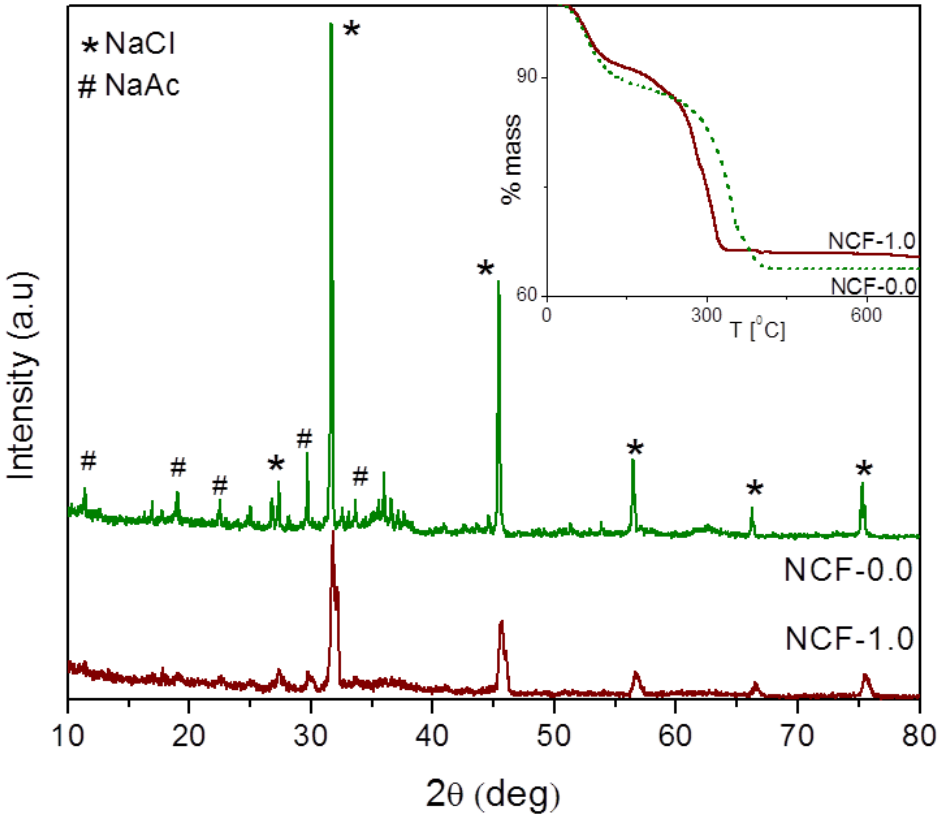
* NaCl
# NaAc
Intensity (a.u)
2θ (deg)
NCF-0.0
NCF-1.0
% mass
T [°C]
90
60
0
300
600
10
20
30
40
50
60
70
80

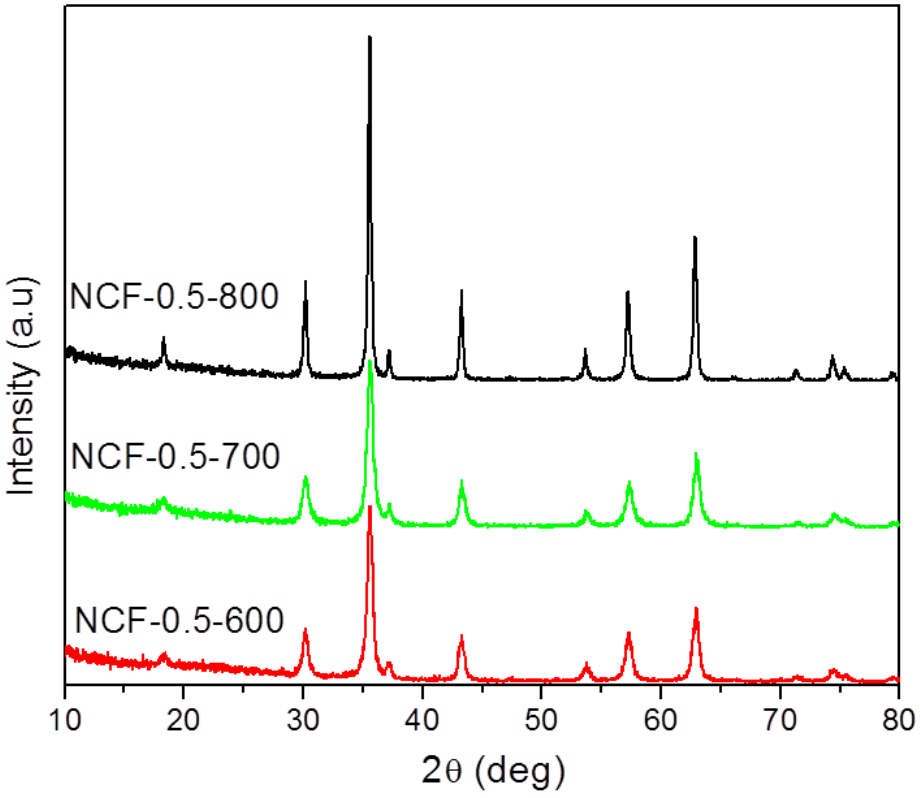
NCF-0.5-800
NCF-0.5-700
NCF-0.5-600
Intensity (a.u)
10
20
30
40
50
60
70
80
2θ (deg)

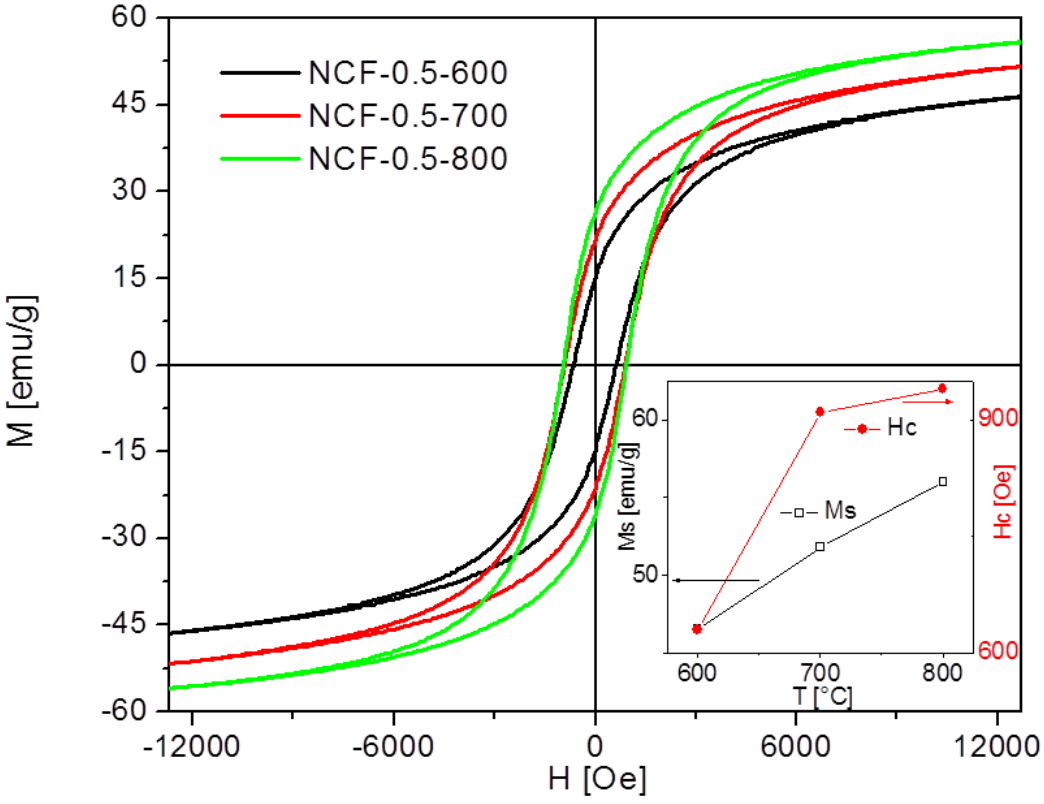
NCF-0.5-600
NCF-0.5-700
NCF-0.5-800
M [emu/g]
H [Oe]
60
45
30
15
0
-15
-30
-45
-60
-12000
-6000
0
6000
12000
Hc
Ms
Ms [emu/g]
Hc [Oe]
T [°C]
600
700
800
900

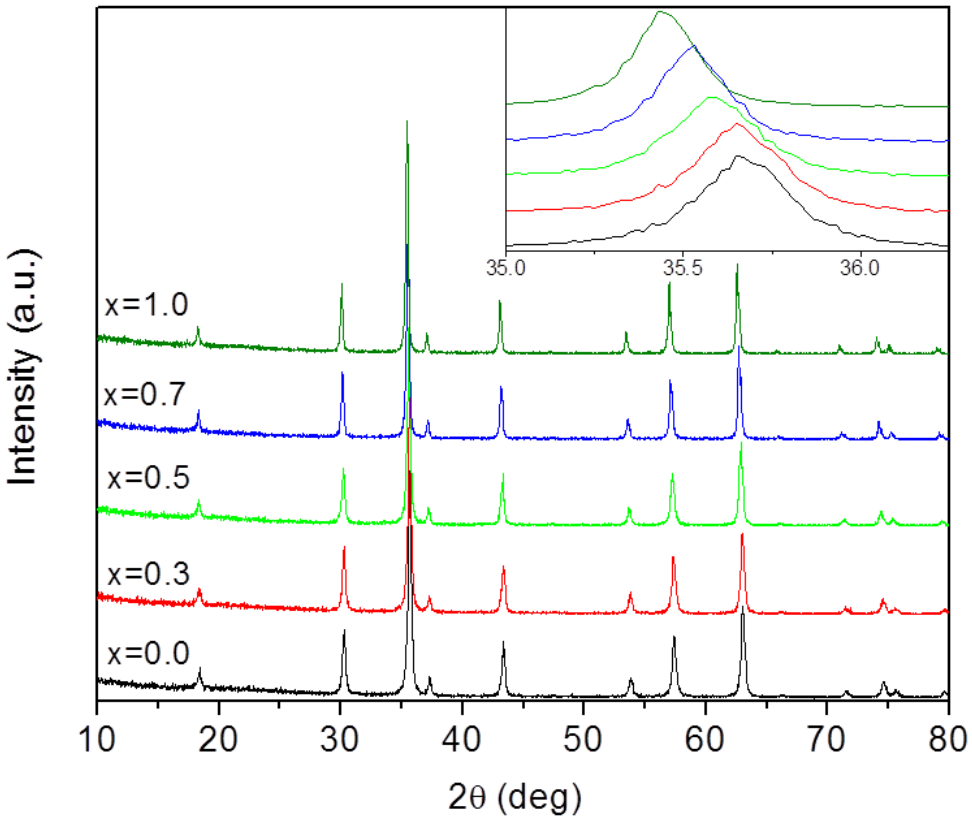
Intensity (a.u.)
x=1.0
x=0.7
x=0.5
x=0.3
x=0.0
10
20
30
40
50
60
70
80
2θ (deg)
35.0
35.5
36.0

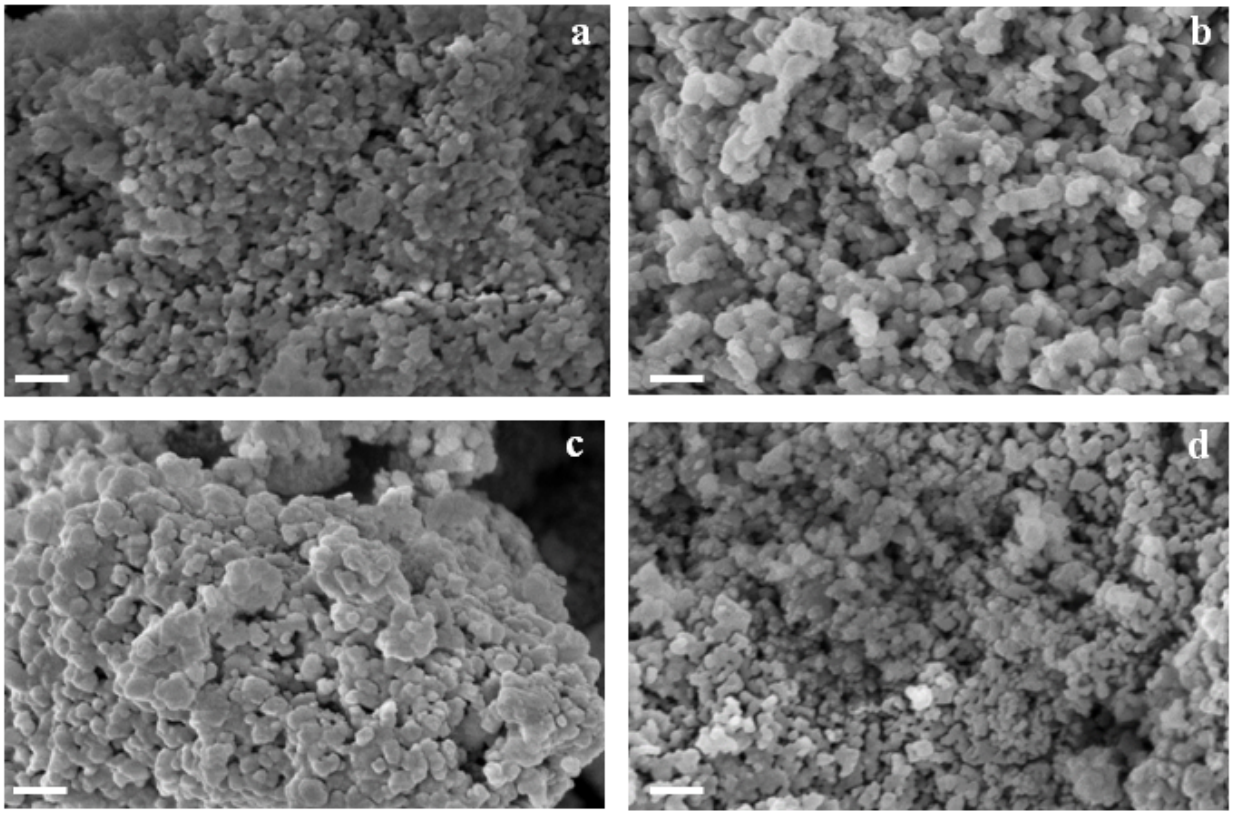

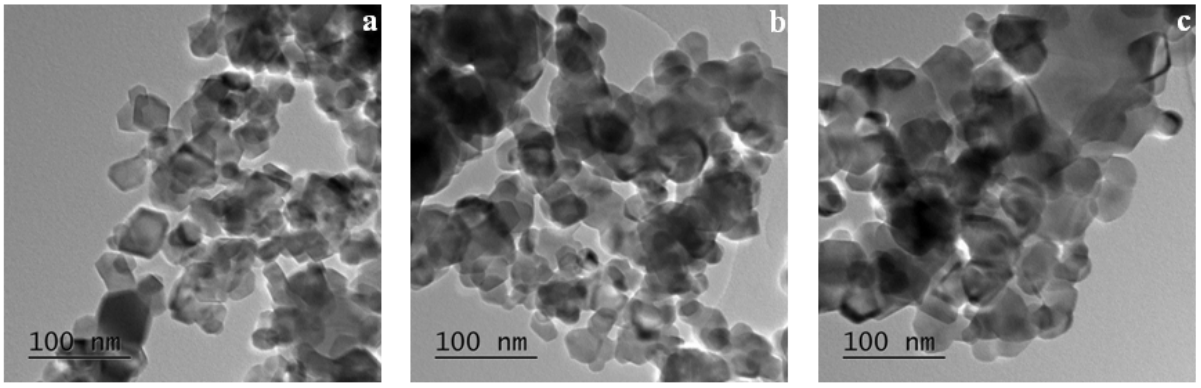

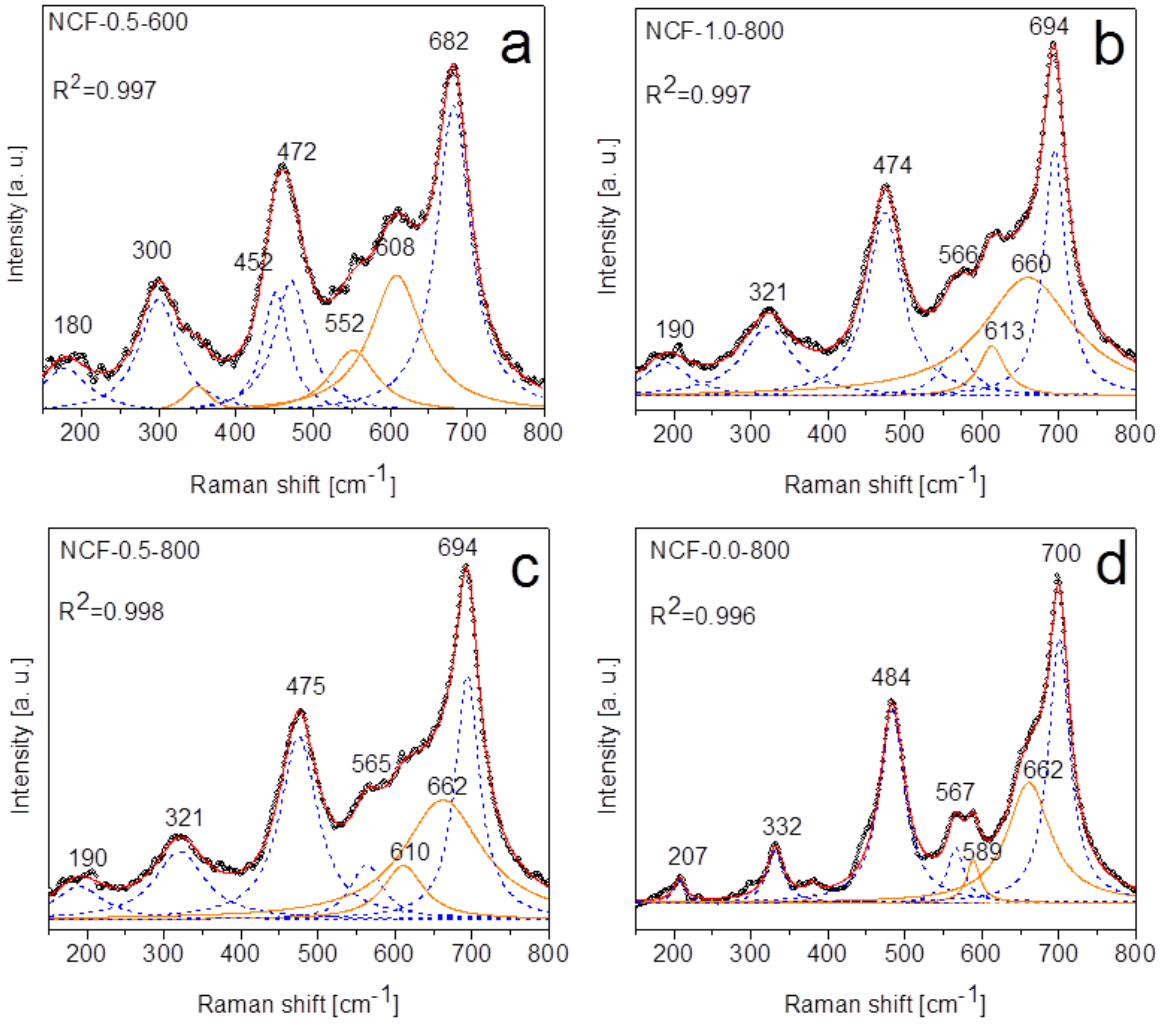
NCF-0.5-600
R^2=0.997
a
682
472
300
452
608
552
180
NCF-1.0-800
R^2=0.997
b
694
474
566
660
321
613
190
NCF-0.5-800
R^2=0.998
c
694
475
565
662
321
610
190
NCF-0.0-800
R^2=0.996
d
700
484
567
662
332
589
207
Intensity [a. u.]
Raman shift [cm^{-1}]
200
300
400
500
600
700
800

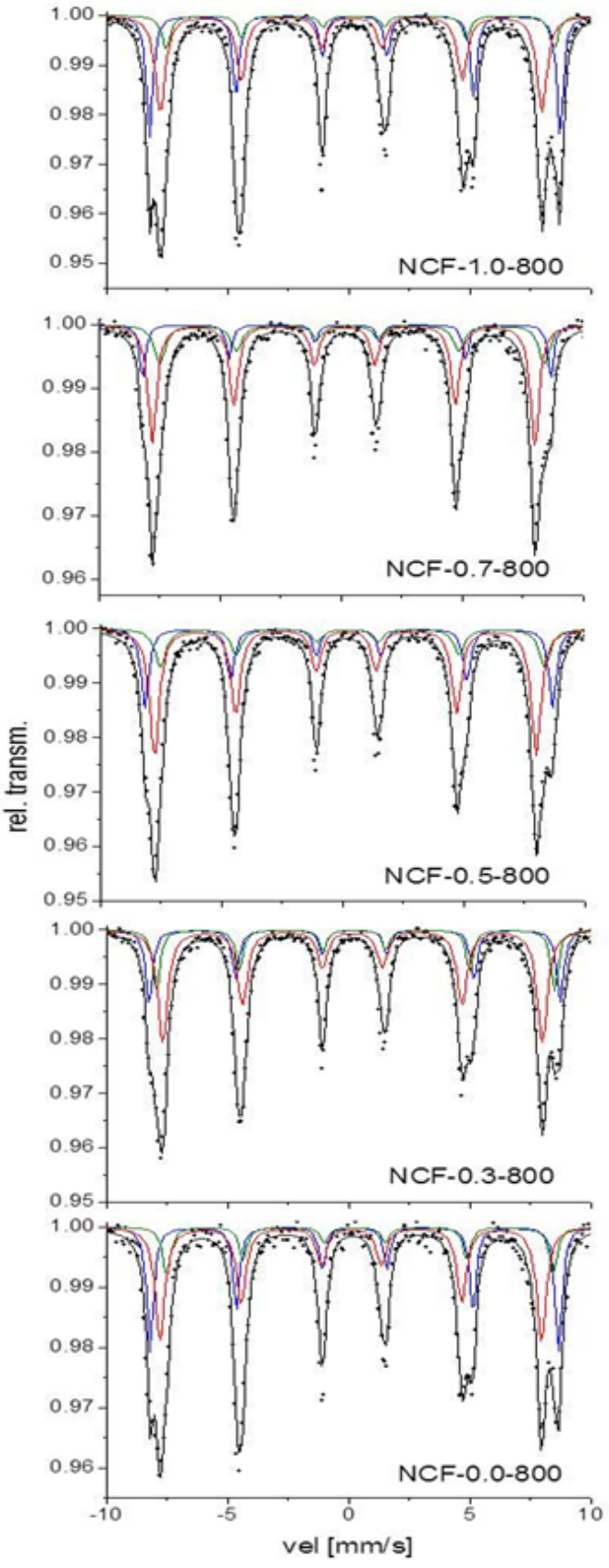

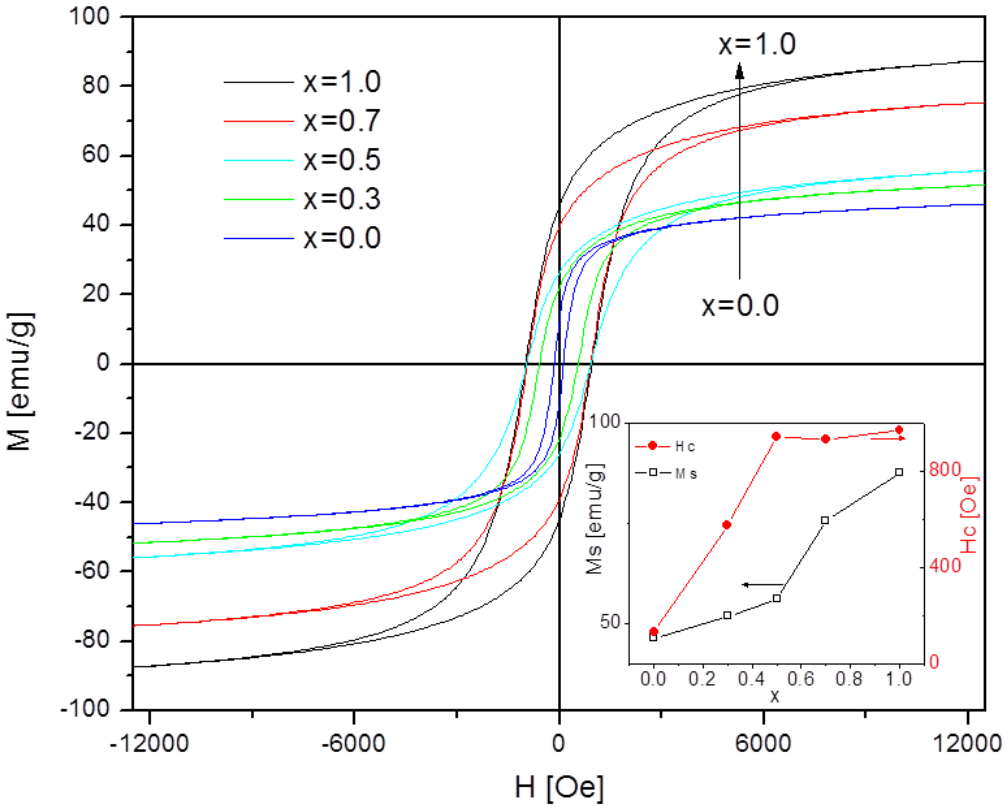
x=1.0
x=0.7
x=0.5
x=0.3
x=0.0
x=1.0
x=0.0
M [emu/g]
H [Oe]
100
80
60
40
20
0
-20
-40
-60
-80
-100
-12000
-6000
0
6000
12000
Hc
Ms
Ms [emu/g]
Hc [Oe]
x
100
50
800
400
0
0.0
0.2
0.4
0.6
0.8
1.0

HIGHLIGHTS

• A mechanochemical acid-base reaction yields $Ni_{1-x}Co_xFeO_4$ and soluble byproducts at room temperature

• Ulterior heating and washing produce pure nanocrystalline ferrite phase for all the compositions

• Changes in the composition influence the crystal structure and magnetic properties of the materials

• Magnetic properties vary mainly with the particle size and cation distribution in the lattice

• The magnetic structure is interpreted as two local fields for the Fe^{3+} sites, variable with composition